Non-invasive Characterisation of Macroreentrant Atrial Tachycardia Types from a Vectorcardiographic Approach with the Slow Conduction Region as a Cornerstone

Samuel Ruipérez-Campillo, Sergio Castrejón, Marcel Martínez, Raquel Cervigón, Olivier Meste, José Luis Merino, José Millet, Francisco Castells

Non-invasive characterisation of macroreentrant atrial tachycardia types from a vectorcardiographic approach with the slow conduction region as a cornerstone

Journal Article

Author(s):
Ruipérez-Campillo, Samuel; Castrejón, Sergio; Martínez, Marcel; Cervigón, Raquel; Meste, Olivier; Merino, José L.; Millet, José; Castells, Francisco

Publication date:
2021-03

Permanent link:
https://doi.org/10.3929/ethz-b-000468186

Originally published in:
Computer Methods and Programs in Biomedicine 200, https://doi.org/10.1016/j.cmpb.2021.105932

Computer Methods and Programs in Biomedicine 200 (2021) 105932

Contents lists available at ScienceDirect

Computer Methods and Programs in Biomedicine

journal homepage: www.elsevier.com/locate/cmpb

Non-invasive characterisation of macroreentrant atrial tachycardia types from a vectorcardiographic approach with the slow conduction region as a cornerstone

Samuel Ruipérez-Campillo[a,c,d,1,*], Sergio Castrejón[b], Marcel Martínez[b], Raquel Cervigón[e], Olivier Meste[f], José Luis Merino[b], José Millet[a], Francisco Castells[a,*]

[a] ITACA Institute, Universitat Politècnica de València, Valencia, Spain
[b] Unidad de Arritmias y Electrofisiología Robotizada, Hospital Universitario La Paz, IdiPaz, Universidad Autónoma, Madrid, Spain
[c] Department of Information Technology and Electrical Engineering, Swiss Federal Institute of Technology (ETH), Zürich, Zürich, Switzerland
[d] Department of Bioengineering and Aeroespace Engineering, Universidad Carlos III de Madrid, Madrid, Spain
[e] Escuela Politécnica, Universidad de Castilla la Mancha, Cuenca, Spain
[f] Université Cote d'Azur, CNRS, Lab. I3S, Sophia Antipolis, France

ARTICLE INFO

Article history:
Received 24 September 2020
Accepted 4 January 2021

Keywords:
Atrial flutter
Vectorcardiogram
Ablation
Macroreentrant atrial tachyarrhythmia

ABSTRACT

Background and objectives: Macroreentrant atrial tachyarrhythmias (MRATs) can be caused by different reentrant circuits. The treatment for each MRAT type may require ablation at different sites, either at the right or left atria. Unfortunately, the reentrant circuit that drives the arrhythmia cannot be ascertained previous to the electrophysiological intervention.

Methods: A noninvasive approach based on the comparison of atrial vectorcardiogram (VCG) loops is proposed. An archetype for each group was created, which served as a reference to measure the similarity between loops. Methods were tested in a variety of simulations and real data obtained from the most common right (peritricuspid) and left (perimitral) macroreentrant circuits, each divided into clockwise and counterclockwise subgroups. Adenosine was administered to patients to induce transient AV block, allowing the recording of the atrial signal without the interference of ventricular signals. From the vectorcardiogram, we measured intrapatient loop consistence, similarity of the pathway to archetypes, characterisation of slow velocity regions and pathway complexity.

Results: Results show a considerably higher similarity with the loop of its corresponding archetype, in both simulations and real data. We found the capacity of the vectorcardiogram to reflect a slow velocity region, consistent with the mechanisms of MRAT, and the role that it plays in the characterisation of the reentrant circuit. The intra-patient loop consistence was over 0.85 for all clinical cases while the similarity of the pathway to archetypes was found to be 0.85 ± 0.03, 0.95 ± 0.03, 0.87 ± 0.04 and 0.91 ± 0.02 for the different MRAT types (and $p < 0.02$ for 3 of the 4 groups), and pathway complexity also allowed to discriminate among cases (with $p < 0.05$).

Conclusions: We conclude that the presented methodology allows us to differentiate between the most common forms of right and left MRATs and predict the existence and location of a slow conduction zone. This approach may be useful in planning ablation procedures in advance.

1. Introduction

Macroreentrant atrial tachyarrhythmia (MRAT), commonly known as atrial flutter (AFL), is the second most common atrial tachyarrhythmia and is becoming increasingly prevalent [1,2]. Catheter ablation is the most common treatment [3]. However MRAT is physiologically caused by a macroreentrant electro-

* Corresponding authors at: ITACA Institute, Universitat Politècnica de Valencia, Camino de Vera s/n, Valencia 46022, Spain
E-mail addresses: samuel.ruiperez@alumnos.uc3m.es, sruiperez@student.ethz.ch (S. Ruipérez-Campillo), fcastells@eln.upv.es (F. Castells).
[1] The first author of this academic publication is S. Ruipérez-Campillo.

https://doi.org/10.1016/j.cmpb.2021.105932

physiological circuit at the atria, which usually follows a path surrounding one or more anatomic obstacles [4]. The most frequent MRAT type, also known as typical AFL, follows a common pattern located at the right atrium, where the activation path surrounds the tricuspid valve [5], in any of the two possible directions, either clockwise (CW) or counterclockwise (CCW) [6]. Atrial activation in typical AFL passes through an isthmus with slow conduction as a distinctive feature, which favours perpetuation of the macroreentry, as it allows the full repolarisation of the atrial myocytes once the refractory period is over. Once ready for a new activation, subsequent cycles are repeated steadily and periodically [7,8]. Ablation of the cavotricuspid isthmus creates a line of conduction block which terminates typical AFL and renders it no longer inducible [9]. Although some other options have recently been proposed [10], the radiofrequency ablation of the cavotricuspid isthmus is a well defined treatment [11].

Beyond typical AFL, other circuits may also cause sustained atrial macro reentries, which otherwise will require different ablation interventions. Hence, MRAT can be classified into different MRAT types [12], where typical AFL is the most prevalent (90%), whereas the other cases are usually denoted as atypical AFL. In recent times, the use of electroanatomical mapping systems allows for the integration of electrical activation data of the atria on computerised 3D anatomical models of the atria. This has facilitated mapping and ablation of these arrhythmia but is still a time consuming procedure which requires expertise and training. Although ECG Imaging (ECGI) is a promising noninvasive mapping technique, it is not widely employed in clinical settings yet and its results are controversial [13,14].

Therefore, a method to distinguish different atypical flutter types and identify the most probable reentrant circuit from the ECG would be valuable in order to obtain key information prior to the electrophysiological study. Identifying whether the MRAT is from the left or right atrium is of great help as it facilitates to planning in sense of either maintaining treatment with medicines or referring them to the appropriate facility in case of ongoing MRAT. The other essential advantage would be simplifying the electroantomical mapping by directing the physician to the area of interest - and thus avoid starting from scratch.

Though first described more than a century ago [15], the mechanisms and techniques used for AFL diagnosis have seen little more than minor changes in practice. Traditionally, diagnosis relied heavily on the twelve-lead electrocardiogram (ECG) analysis and the distinctive atrial waves in leads II, III, aVF, aVL, V1,V2, characterised by continuous and regular saw-tooth waveforms with cycle lengths of around 250 ms [5]. In 2001, more than three decades after the first classification of AFL, the European Society of Cardiology and the North American Society of Pacing and Electrophysiology developed the current classification of the arrhythmia [16]. Although the analysis of ECG is used to detect flutter cases [17], waveform variants, such as positive or biphasic waves, that have been proven to exist, are not easily associated with different MRAT types [18]. Thus, ECG is merely orientative, even for typical AFL cases, as false positives and negatives are commonly registered.

A major hindrance for MRAT diagnosis is that most patients present a 2:1 atrio-ventricular conduction ratio. Consequently, the atrial wave is overlapped by the ventricular components (either the QRS complex or the T-wave). In those cases, the atrial wave is no longer visible unless there is a longer RR interval (e.g. with a 4:1 conduction ratio). Although several methods to cancel the ventricular activity in atrial fibrillation signals have been proposed in the literature [19,20], these are not applicable to MRAT signals, as atrial and ventricular components are coupled. Therefore, in the attempt to remove the QRS-T, the atrial signal is likely to be subtracted as well. Moreover, the strategy based on Blind Source Separation [21,22], which provides one atrial source free from ventricular components –also in MRAT– is insufficient for this purpose, as three independent atrial components would be required to reconstruct the VCG loop. As a result, the unequivocal retrieval of the atrial signal in MRAT recordings still remains a technical challenge [23]. This limitation, however, can be overcome by blocking the AV node during a short period of time, e.g. by administering adenosine [24].

Apart from ECG interpretation, the vectorcardiographic approach [25], sustained on the dipolar nature of the heart, was defined for the representation of 3-dimensional surface loops. Quantitative measurements, such as planarity, plane orientation, loop roundness or the vector with maximum amplitude, among others, have been defined to assess the morphology of the QRS loop [26,27]. Moreover, the QRS-T angle has been associated with the risk of sudden cardiac death [28]. With respect to MRAT, VCGs have also been described [29,30], but no clear correlation has been demonstrated for proven mechanisms. Unlike P, QRS or T waves, which are caused by synchronised depolarisation/repolarisation of the myocytes following a rest period with isoelectric potential, in MRAT, the atrial signal is a result of a continuous activation. Accordingly, atrial VCGs lack coordinates for the origin of activation. Hence, as MRAT loops differ in their generation mechanisms from P loops, novel features, specifically conceived for MRAT, should be explored to extract clinically meaningful information.

In this study, we hypothesise that there is a correlation between the atrial VCG loops and the type of atrial flutter that the patient suffers. This correlation is thought to be strongly related to the distribution of slow conduction areas at the left atrium. Thus, differences in the VCG loop patterns will be studied to characterise the MRAT archetype defined for each group.

2. Study design

In order to prove our hypothesis, we developed a method based on a new perspective of the VCG signal, where the evolution of the dipole direction and the slow conduction regions play a significant role. This method was tested from different standpoints. On the one hand, we evaluated the properties of the methods using simulations. Several simulation strategies have been employed to test methods forprocessing cardiac signals, including geometrical models [31], signal synthesis from the combination of periodic components [32], semi-synthetic signals from the manipulation and combination of real signals [22] and computational methods based on physiological properties, as used in Lemay et al. [33]. In this study, we used a geometrical model, which allows for a full control and parametrisation of the 3D loop described by the vector and the location of the slow conduction regions. A synthetic VCG generator was designed, based on a mathematical model to support the methods used for the analysis and the posited hypothesis. On the other hand, a prospective study was designed to test the methods on MRAT patients. Patients were recruited at the Robotic Cardiac Electrophysiology and Arrhythmia Unit, at the Hospital Universitario La Paz (Madrid, Spain) according to a protocol approved by the hospital's ethics committee. The recruitment protocol was compliant with the Declaration of Helsinki and all patients involved signed consent forms. The classification of the MRAT type was determined after the electrophysiological procedure. Clinical data (ECG measurements) are transformed to VCG signals before feature extraction.

The proposed methodology involved the creation of VCG archetypes for each group and VCG feature extraction parameters to quantify its similarity to an archetype, intra-patient consistence of the atrial VCG loop, the velocity profile of the trajectory and the complexity (i.e. the sinuosity) of the VCG trace. Statistical tests were finally carried out to evaluate the performace of the methods.

3. Materials

3.1. Synthetic data

A geometrical model aiming to generate loops based on distinctive features of atrial VCGs was created. This model highlights the non-uniform velocity of the trajectory and the presence of a slow velocity region. The purpose of the simulations is to contrast the information exploited from the methods with a full control of the geometrical properties of the loops.

Bearing in mind that diverse reentry circuits with different plane orientation, location of the slow region and rotation sense may exist, 8 archetypes defined according to those characteristics were defined. The variability of loops belonging to the same group was considered by introducing a wide range of randomized variables, such as shape, plane rotation, spatial shifts of the slow velocity region and complex curvatures in the pathway.The model adopts a geometrical approach with random parameters following a uniform distribution between ranges empirically found in VCGs from MRAT patients.

The generation of the VCG loops starts with the definition of an ellipse. From the Euler expression, the relationship between major and minor semi-axes are randomised within a range of values. It is worth mentioning here that, when discretising the XYZ projections or signals according to the constant sampling period, the spatial discretisation of the elliptical figures entails a higher density of points near the minor semi-axis, so that the spatial velocity of the trajectory described by the loop is not constant along the entire path. However, this should not be regarded as a limitation, but rather an asset of the model, as variations of the velocity profile also appear in real MRAT VCG loops.

Taking a deeper look at the idea of forcing a more pronounced slow velocity region as a characteristic feature, a non-uniform discretisation of the angle is obtained from:

$$\Delta\theta_n = \alpha\left|\cos\left(n\frac{\pi}{N}+\phi\right)\right| + \Delta\theta_{\min}, \tag{1}$$

where $\Delta\theta_n$ is the angular increment at each n sample, N is the total number of samples of the loop, $\Delta\theta_{\min}$ is the minimum angle increment, which sets up the minimum velocity, $\alpha + \Delta\theta_{\min}$ is maximum angle variation, which stands for high velocity regions, and the phase argument ϕ determines the location of rapid and slow regions. The parameters in Eq. (1) must fulfill the constraint that the accumulated angle increment throughout the entire loop equals 2π. Accordingly, if a lower $\Delta\theta_{\min}$ is desired, α must be increased to fulfill that condition, as one parameter relies on the other. Overall, choosing one of them will directly fix the velocity balance between rapid and slow regions.

To create a wide variety of loop shapes with meanders, curvature variations and avoiding strict confinement within a plane, the vector modulus (radius of the projections), which depends on the angle and the semi-axes, is varied by means of weighted (Q_1, Q_2 and Q_3) frequency modulating functions (C_1, C_2 and C_3), so that:

$$r(\theta) = \frac{a\cdot b}{\sqrt{\left(a\cdot\cos(\theta)+Q_1C_1\right)^2+\left(b\cdot\sin(\theta)+Q_2C_2\right)^2+Q_3C_3}} \tag{2}$$

This allowed a wide range of combinations of large arc deviations and small but rapid oscillations. A similar modulation vector is also defined in the perpendicular plane of the ellipse, thereby allowing the path to run out of the main plane. As a result, a curvature throughout all 3 dimensions is generated.

In order to avoid possible sharp peaks in the velocity profile (which may occasionally appear) a low-pass filter is applied over the 3-dimensional path. An adaptation of the Savitzky-Golay filter over the three axes was implemented [34] to make the trajectory smoother and avoid these possible peaks. Finally, the spatial orientation of the loop is set by means of a geometric rotation of the three axes. An example of a synthetic VCG loop is represented in Fig. 1.

With this model, 4 different groups were defined, according to the location of the slow region and with different loop orientations. On average, the location of the slow region was set at every 90° for the different groups. With regard to plane orientation, the loops were rotated with ±40º per coordinate, with some overlapping between groups. Moreover, each group was then divided into two, according to the direction of the trajectory, either CW or CCW. Both versions were considered as independent groups for VCG analysis, thereby generating loops classified into 8 groups (groups 1 to 4 and 5 to 8 corresponding to either CW or CCW versions, respectively). A summary of the parameters and degrees of freedom from the model is depicted in Table 1.

3.2. Clinical data

After the protocol approval, 30 consecutive MRAT patients submitted to an electrophysiological intervention were included in the study. ECG and EGM data was registered by a polygraph (Labsystem pro, Bard, Boston Scientific) with a sampling frequency of 1KHz. Data generated by the electro-navigator during the intervention were recorded and synchronised with the polygraph for the subsequent analysis and description of the gold standard. During ECG registration, adenosine was administered in order to temporally block the atrio-ventricular conduction and hence, obtain pure atrial signals free from any ventricular component. From the outcomes of the electrophysiological intervention, patients were grouped as follows: CW typical AFL (5), CCW typical AFL (6), CW perimitral MRAT (3) and CCW perimitral MRAT (8). The remaining 8 patients were identified as periveins (either pulmonar or cavae) or other MRAT forms, and were included in a miscellaneous MRAT group. In this study, data from patients with anatomical problems or a long history of cardiac disease were disregarded for the statistical analysis. In addition to the ECG data, the results of the electrophysiological studies were available for all patients and considered as the gold standard that identified the macroreentrant circuit —and thus, the MRAT type. An example of an electroanatomical mapping with the activation sequence of a perimitral MRAT is shown in Fig. 2.

4. Methods

4.1. Preprocessing

4.1.1. Atrial VCG loops computing

From the ECG recordings, only the segments under the effects of adenosine depicting a saw-tooth waveform with no ventricular contractions were selected. These signals were bandpass filtered between 1 Hz and 30 Hz to reduce thermal noise and remove the baseline wandering whilst preserving the atrial content intact. Signals were filtered bidirectionally to minimise transient distortion. The atrial cycle length was computed from the first maximum of the atrial signal's autocorrelation function. Having estimated this period, an excerpt with 10 cycles was delimited (Fig. 3A). Subsequently, the signal was split into 10 segments, each of them lasting one exact atrial cycle length.

The VCG was then obtained according to the Inverse Dower's Transform [35] to estimate Frank's leads from the standard ECG system, as this is the most commonly used transformation, although other vectorcardiographic transformations have also been proposed [36].

4.1.2. VCG loop consistence

The consistence assesses the similarity amongst intrapatient atrial VCG loops. Thus, it allows us to determine their repeatabil-

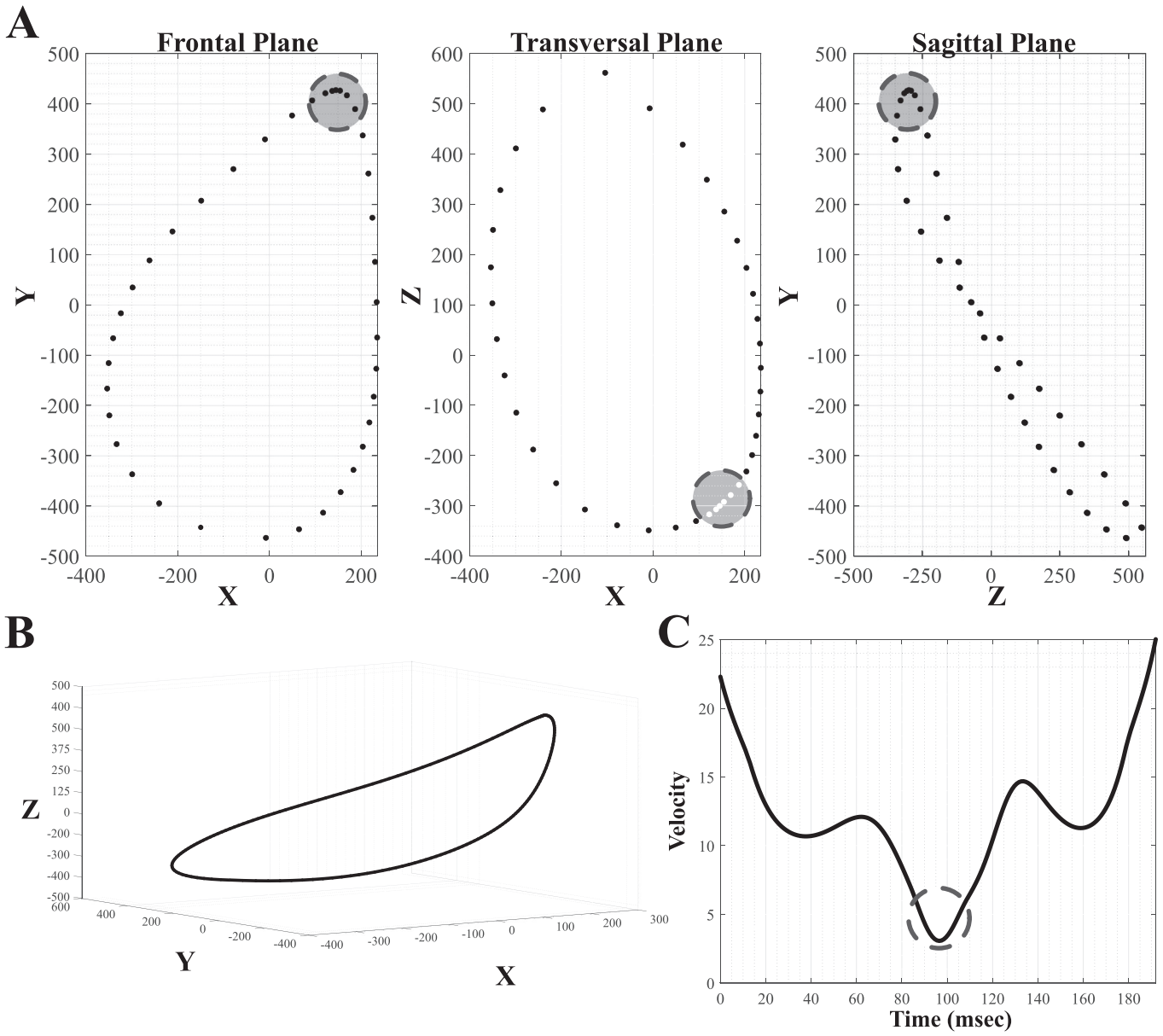

Fig. 1. Example of a simulated VCG. A. Frontal, transversal and sagittal planes. B. 3D representation. C. Velocity profile.

Table 1
Summary of the parameters, description and values in the synthetic model.

Category	Param.	Description	Range
Ellipse Geometry	Perimeter	[2000, 2500]	
	c	Constant maintaining semi-axes (a and b) relation between a range to keep an elliptical shape.	$[1/\sqrt{10}\pi, \sqrt{2}/\sqrt{13}\pi]$
	b	Minor semi-axis. Note that this parameter is not independent.	b = c·P
	a	Major semi-axis. Note that this parameter is not independent.	[1.5b,2b]
	α	Maximum angular displacement (constrains maximum velocity).	[0.3,0.7]
Configuration of the Low Velocity Region	$\Delta\theta_{min}$	Minimum angular displacement (constrains minimum velocity) [rad].	$[10^{-2}, 10^{-4}]$
	Initial angle	Location of the low velocity region	Types 1,2,5 and 6: 0° Types 3,4,7 and 8: 180°
Creating a Winding Pathway	C1Q1	Variation over the major semi-axis	[0,150]
	C2Q2	Variation over the minor semi-axis	[0,150]
	C3Q3	Overall variation (over the radius).	[0,15]
Plane Rotations	X axis	Types 1 and 5: [40°, 80°] Types 2 and 6: [10°, 50°] Types 3 and 7: [10°, 50°] Types 4 and 8: [40°, 80°]	
	Y axis	Types 1 and 5: [70°, 110°] Types 2 and 6: [40°, 80°] Types 3 and 7: [40°, 80°] Types 4 and 8: [70°, 110°]	
	Z axis	Types 1 and 5: [20°, 60°] Types 2 and 6: [10°, 30°] Types 3 and 7: [10°, 30°] Types 4 and 8: [20°, 60°]	
Sense of Rotation	CW	Types 1–4	
	CCW	Types 5–8	

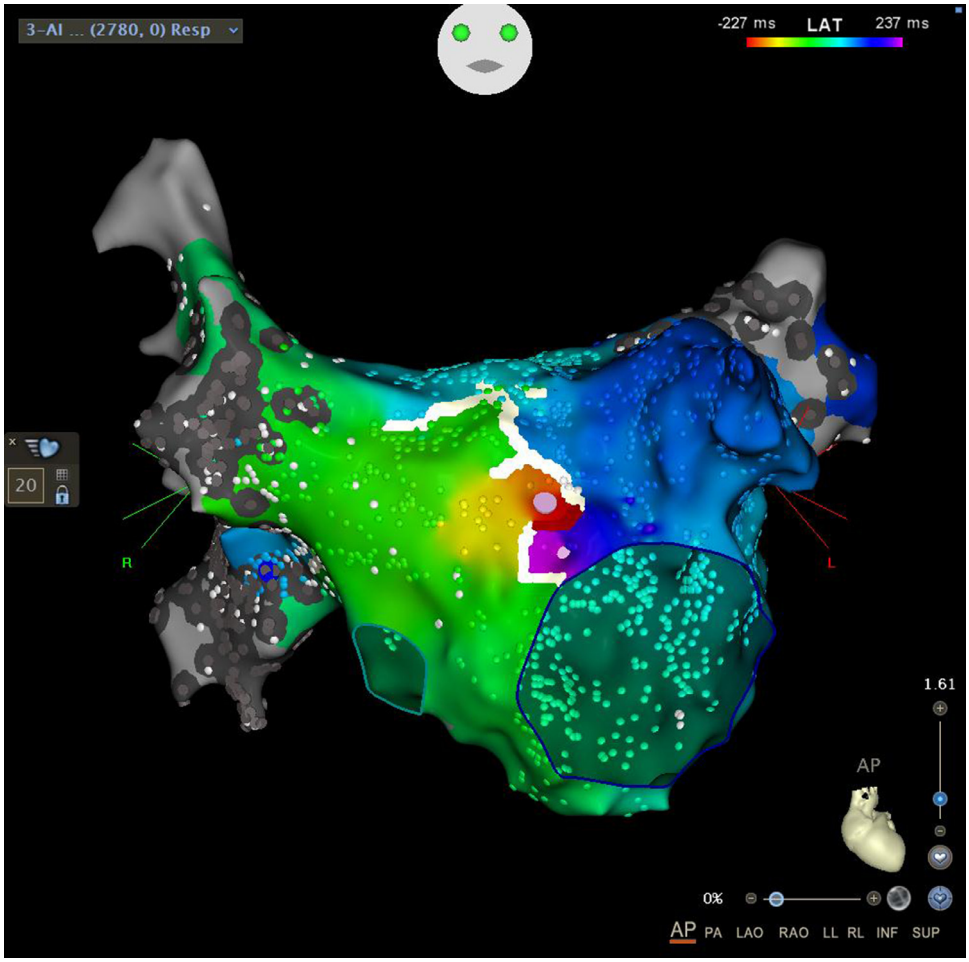

Fig. 2. Electroanatomical mapping with the activation sequence of a perimitral MRAT. The area in red corresponds to the slow conduction region (see the video in the supplementary material to reproduce the activation sequence). The electrophysiological study was used as the gold standard to identify the reentrant circuit and hence the MRAT type. This figure was generated by CARTO®3, Biosense Webster.

ity, which could be impaired due to either the variability of the macroreentrant circuit, the quality of the signal (i.e. signal-to-noise ratio) or respiration [29].

Taking 10 VCG loops for each patient, the consistence is computed from the Eigen Value Decomposition [37], which outputs 10 orthogonal vectors with decreasing representation in terms of variance to the input data. Consistence is then defined as the percentage of variance explained by the most representative component. As macroreentrant circuits in MRAT are repeatable events, consistence values close to 1 are expected in practically all cases, unless a corrupted signal or an unstable circuit is present. Outliers with clearly low consistence values were excluded from the analysis.

4.1.3. Averaged VCG loops

The VCGs from all cycles were averaged to create a representative single-loop VCG signal for a patient (see Fig. 3). As the atrial cycle length will be different for each patient, and with the aim of allowing interpatient VCG loop comparison, XYZ components were resampled so that the averaged VCG had the same number of samples in all patients (in this study we considered 500 samples, although this number is not a critical point).

4.2. VCG archetypes

In order to identify the MRAT type for a given patient, a representative VCG for each group would be required, so that the similarity to each VCG pattern could be obtained and therefore determine the greater similarity of MRAT to an unknown VCG. To this end, the VCGs were divided into different groups (both in simulations and real data), VCG archetypes are created from the average of time aligned VCGs. In order to prevent excessive amplitudes of ECG signals, all VCGs were previously normalised so that their respective vectors had the same averaged modulus along the entire loop. The ensemble of VCG loops belonging to the same MRAT group was jointly aligned according to a least squares minimisation approach described in the Appendix.

4.3. Characterisation of VCG loops

Vectorcardiographic signals have been previously characterised [38]. The new approach described below was applied to both simulated and real data. Before any feature extraction and for every VCG, the mean value was firstly removed from all three Cartesian axes, so that the loop was spatially repositioned towards its centre of gravity –notice that it will be closer to the low-velocity region, as it has a higher density of samples.

4.3.1. Similarity between VCG loop pairs

In order to assess the similarity between VCG loop pairs, the 3-dimensional VCG vectors were correlated sample-by-sample until all N vectors that make up each loop were compared. The similarity between two loops is hence defined as:

$$S = \frac{1}{N}\sum_{i=1}^{N}\frac{\mathbf{x}_i^T\mathbf{y}_i}{\|\mathbf{x}_i\|\|\mathbf{y}_i\|}, \tag{3}$$

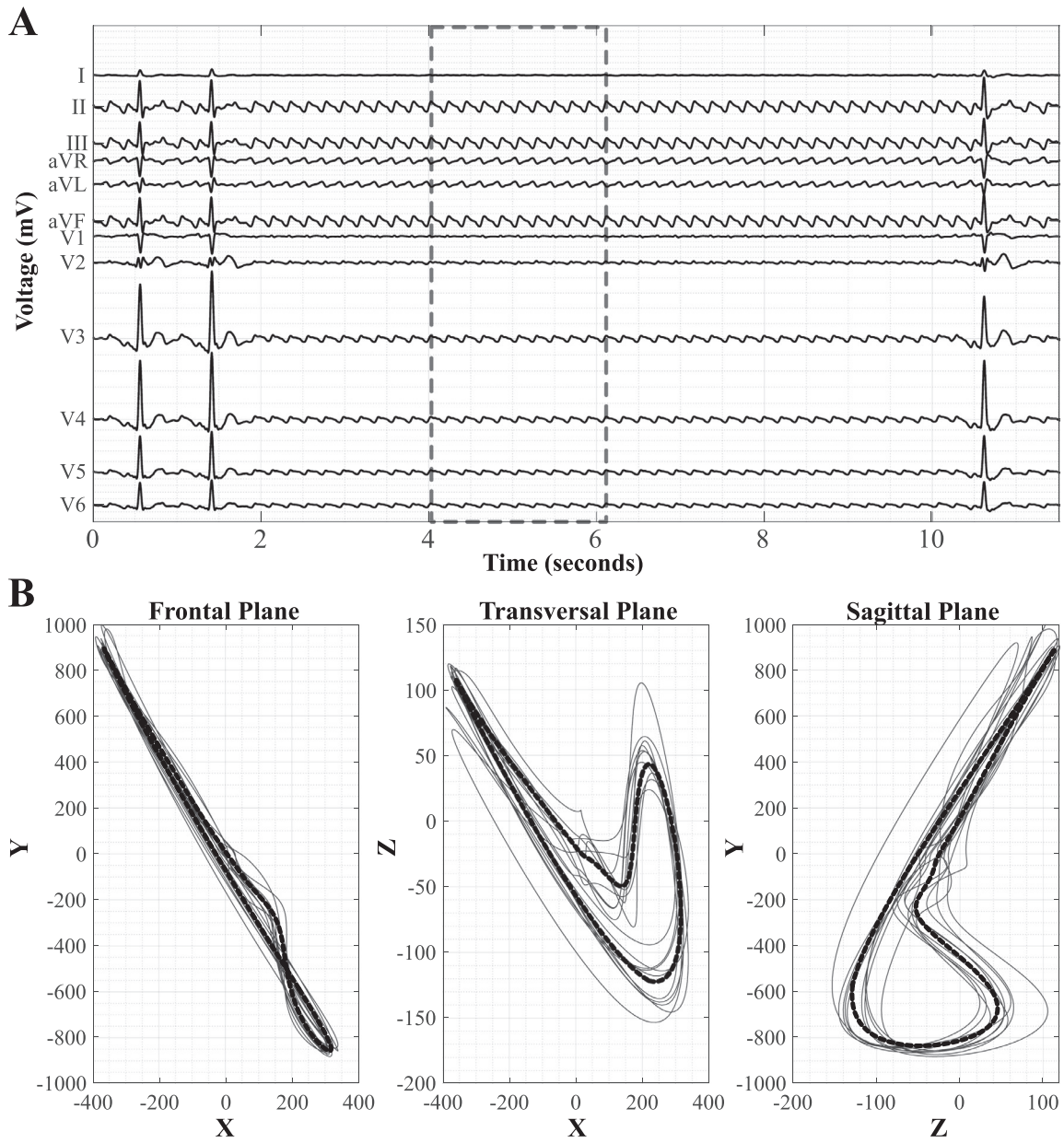

Fig. 3. A: 12-lead ECG signal from a typical CCW AFL under the effects of adenosine. Notice large RR segments due to AV blockage. B: VCGs reconstructed from 10 consecutive atrial cycles are superimposed (see region in the dashed box in A), with the averaged VCG in thick dashed trace.

where $\mathbf{x}_i$ and $\mathbf{y}_i$ are the 3-dimensional vectors of each VCG loop, respectively, at the ith sample and N is the total number of samples, which is the same in both loops since they were previously resampled as mentioned before. Notice that, in this definition, the similarity is not affected by differences in the amplitude of the vectors, but relies solely on the direction the vectors are pointing to. As the slow regions have a higher spatial density of samples, they will be over-weighted with respect to other regions and thus, play a key role in this parameter. In other words, two VCGs decribing exactly the same path but with different locations of the slow region will not have a similarity of 100%. Otherwise, two VCGs describing different paths but with roughly the same location of slow regions may have a higher similarity than visually expected.

It is worth mentioning that special care must be taken in the alignment of the loops, as misaligned loops would erroneously provide low correlation values. Therefore, the similarity parameter S is in fact a cost function $S(k)$, which depends on the loop alignment, where k is the number of samples by which the second loop is shifted, taking N possibilities, from 0 to $N-1$. Due to the variability of MRAT loops, particularly if they come from different MRAT types, we cannot a priori estimate the shape of the cost function. The possible existence of local maxima at which a maximisation function could become anchored is unknown. For this reason, anywhere that the similarity between loops is computed in this study, all possible N shifts will be considered, taking the absolute maximum $S_{\max}$. As subsequently reported in the results section on the cost function shape, in later studies a maximisation function could be applied with the aim of carrying out fewer iterations hence saving computational load.

4.3.2. Identification of the Most Similar archetype

For each VCG, the similarity to each archetype was computed as described in Sections 4.3 and 4.3.1. The highest coefficient will determine which group it is closest to. In the case of real data, due to the low number of patients in each group, and in order to en-

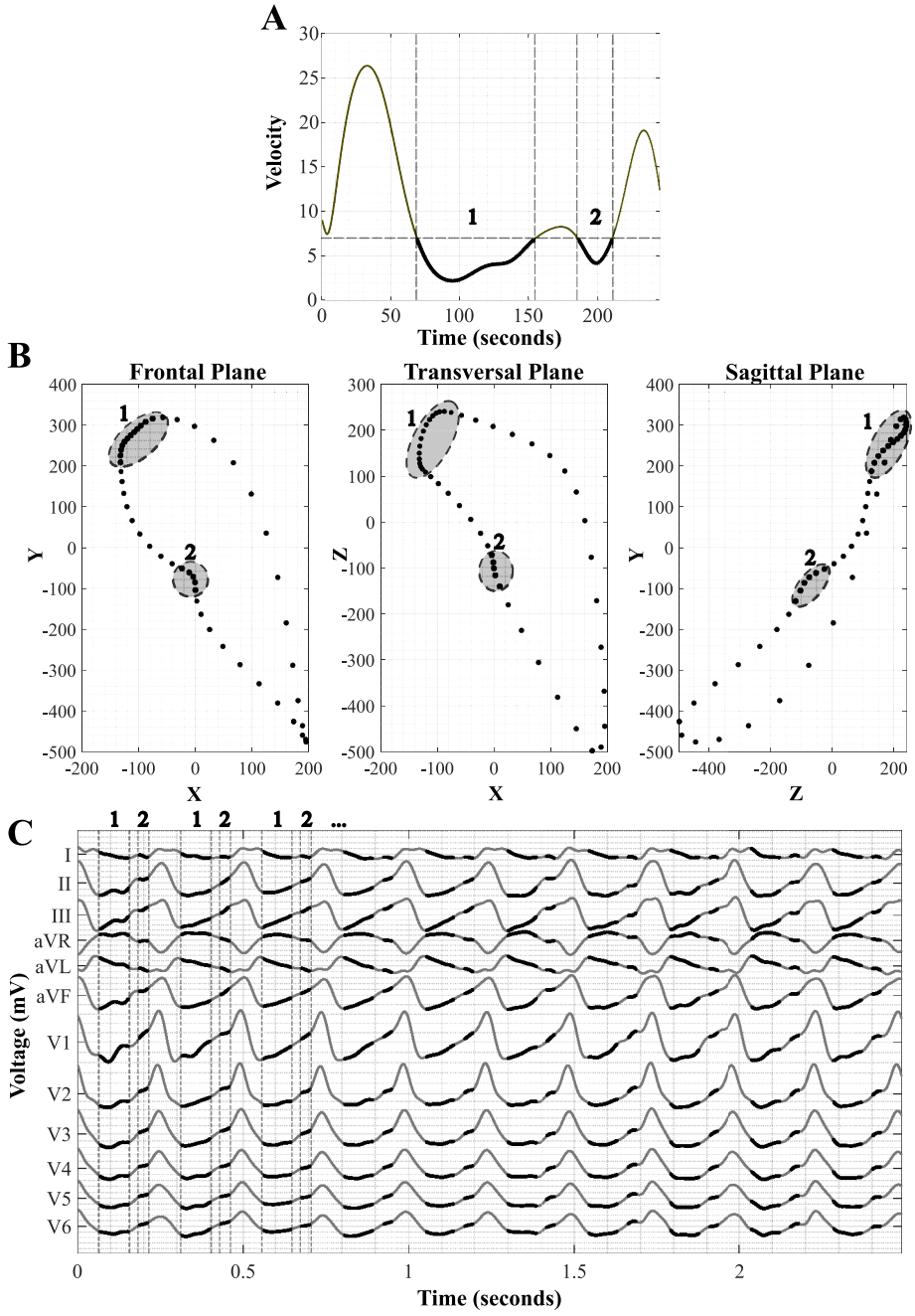

Fig. 4. A. Primary and secondary slow velocity intervals, labelled as 1 and 2, respectively, are detected in a Perimitral CCW MRAT. B. Slow velocity regions are highlighted in VCG projections. C. Highlight of slow velocity intervals on the atrial ECG signal. These intervals correspond to segments with a smoother slope. 10 atrial waves are represented (from which the average VCG loop in B is created). The first three waves are labelled with the two slow conduction region - 1 is the slowest.

sure a fair comparison, the VCG being tested were excluded for the generation of the archetypes following a Leave One Out strategy.

4.3.3. Slow conduction velocity regions

The velocity profile along the loop is computed from the spatial distance between consecutive loop samples. As the units of the VCG leads are given in volts and the temporal scale is expressed in atrial cycles, the resulting units are [V/cycle]. A threshold fixed to a quarter of the maximum velocity was set to identify the VCG sites and the temporal instants associated with slow conduction (see Fig. 4). From this, the following parameters were defined: (1) **T**ime **F**raction during which the trajectory advances at low velocity (TF_{LV}); (2) **D**istance **F**raction outlined during the low velocity period (DF_{LV}) and (3) the ratio between these two parameters, i.e. **T**ime fraction over **D**istance fraction (as a **R**atio) under low velocity conditions (TDR_{LV}).

As MRAT VCGs are closed loops, the angular velocity profile was also computed, in order to enrich and supplement the information provided by the velocity profile. At the ith sample, the angular velocity ω, which is expressed in [rad/s] units, is defined as:

$$\omega_i = \frac{1}{T_s} \arccos\left(\frac{\mathbf{v}_i^T \mathbf{v}_{i+1}}{\|\mathbf{v}_i\| \|\mathbf{v}_{i+1}\|}\right), \tag{4}$$

where $\mathbf{v}_i$ is the 3-dimensional vector at the ith sample and T_s is the sampling period (with required corrections after resampling). To illustrate the interpretation of this parameter, let us consider an MRAT loop with no meanders and a cycle length of 250 ms. In this

case, the expected angular velocity, on average, would be 8π rad/s, as in one second it would complete 4 entire loops, or 1.4 deg/ms. This angular velocity is likely to increase with shorter cycle lengths and/or bending traces.

4.3.4. Complexity of the pathway: quantification of bending traces

This parameter intends to capture local variations in order to evaluate the complexity of the trajectory. The rationale of this parameter is that, the further the pathway bends, with more meanders and direction changes, the higher the complexity of the pathway. Therefore, the complexity can be regarded as the accumulation of the instantaneous angle variation Θ_i, which for the ith sample is computed as:

$$\Theta_i = \arccos\left(\frac{(\mathbf{x}_i - \mathbf{x}_{i-1})^T(\mathbf{x}_{i+1} - \mathbf{x}_i)}{\|\mathbf{x}_i - \mathbf{x}_{i-1}\|\,\|\mathbf{x}_{i+1} - \mathbf{x}_i\|}\right) \quad (5)$$

The accumulation of all angle variations Θ_i along the full pathway is lower bounded by 2π rad, which is the value obtained in the simplest case (i.e. the direction vector makes a complete turn). However, since there is no upper boundary for this parameter and, in order to keep a parameter within a reasonable range, we define the complexity C as:

$$C = 1 - \frac{2\pi}{\sum_i \Theta_i}, \quad (6)$$

which is lower bounded by 0 (the simplest pathway, with no local oscillations) and upper bounded by 1 (in the case of an infinitely complex trajectory).

4.4. Statistical analysis

4.4.1. Synthetic VCGs

A one-way analysis of variance (ANOVA) was calculated on synthetic VCGs. Snedecor's F distribution is applied in analysing variance to see if three or more samples come from populations with the same mean values. The F-ratio and the associated probability value (p-value) are reported. If the p-value associated with the F is less than 0.05, the null hypothesis will be rejected and a multiple comparison test will be carried out. In these cases, post-hoc tests allow us to examine mean comparisons, which can be thought of as a subset of possible contrasts between the means. The Bonferroni method is used for general tests of possible contrasts.

The Receiver Operating Characteristic (ROC) curves were computed for each of the synthetic groups, contrasting sensibility and specificity in a binary classification system. Two sets of data were evaluated, one for each direction. In each of the sets, the cases of the group being evaluated (1000 synthetic VCGs) were contrasted with the other groups (3000 synthetic VCGs). The Area Under the Curve (AUC) was used as the measure to quantify a good classifier to distinguish between each AFL archetype for each group.

4.4.2. Real data

As the patients database represents different distributions, and given the low number of cases, the non-parametric Kruskal-Wallis test was applied - used for more than two independent samples. It is roughly equivalent to a parametric one way ANOVA with the data replaced by their ranks. If the p-value is less than 0.05, the null hypothesis will be rejected.

5. Results

5.1. Synthetic data

5.1.1. Comparison between groups

The similarity parameters were tested for VCG comparison between groups. The ANOVA test shows statistical significance for all the cases for all groups. The F-parameter for each group ranged from $F(3, 3996) = 959.20,\ p < 0.001$ to $F(3, 3996) = 1456.28,\ p < 0.001$. Thus, although overlapping between groups occurs, statistical tests show differences between the types from the evaluation of the correlation parameter. Furthermore, when evaluating through multiple comparisons using Bonferroni's correction, all groups are found to show high statistical significance when compared to any other ($p < 0.001$ for all of them). Fig. 5 shows the boxplot results of the simulation analysis from the set of data of 8000 synthetic cases (i.e. 1000 per group for each of the 8 groups) taken from the database created, as described in Section 3.1 using the tools proposed in Section 4.3.1. Only groups I–IV are represented, as groups V–VIII show the same behaviour, since they are described by the same loops rotating in the opposite direction.

The results of the AUC for each ROC curve computed from both directions (see Fig. 6) are displayed in Table 2.

5.1.2. Influence of the slow regions

Over a controlled synthetic VCG, with the slow region at one end of the major semi-axis and the fast region on the opposite end, rotation around the major semi-axis (slowest and fastest regions remain fixed) presents a decrease in similarity to a value as low as 0.8. On the other side, when rotating with respect to the minor semi-axis (semi-slow regions are fixed while slowest and fastest move), the similarity decreases to 0.3.

5.1.3. Complexity

Over a controlled synthetic VCG, the amplitude of the frequency modulating functions are progressively increased (beginning with zero amplitude, i.e. as a 'perfect ellipse). Complexity measurements from these simulations increase from 0 up to 0.8.

5.2. Real data

5.2.1. Intra-patient consistence

Consistence values were over 0.85 in all cases, with an average of 0.95 ± 0.04. One patient registered a consistence value of 0.55 and therefore, was excluded from the analysis. Fig. 3B shows the superposition of 10 consecutive VCGs for a typical CCW AFL, with the averaged VCG represented by a thick dashed line.

5.2.2. Similarity with archetypes

Archetypes for each group are shown in Fig. 7. The results from the average similarity of individual VCGs with group archetypes (computed according to a LOO algorithm) are detailed in Table 3. For all groups, the highest average similarity corresponded to the archetype of its own group. In all groups, the similarity with their respective archetype was at least 0.85 on average, with a standard deviation of less than 0.05 (see an example of perimitral VCGs in Fig. 8). The statistical results from the Kruskal-Wallis test were as follows: except for perimitral CW MRAT ($p = 0.062$), the results for the other groups were statistically significant. Fig. 8 shows three examples of CCW Perimitral MRAT.

5.2.3. Analysis of slow regions

The detection of low velocity intervals and how they can be projected to VCG and atrial signal plots is illustrated in Fig. 9. The results for the time and distance fractions during low velocity periods (TF_{LV} and DF_{LV}, respectively), as well as the ratio between these two parameters (TDR_{LV}) are summarised in Table 4.

The non-parametric Kruskal–Wallis test over these parameters provide a statistical significance for TF_{LV} ($p = 0.047$) but no statistical significance for DF_{LV} ($p = 0.146$) or TDF_{LV} ($p = 0.698$). Note that the threshold as one fourth of the maximum velocity shows statistical significance among groups ($p = 0.025$).

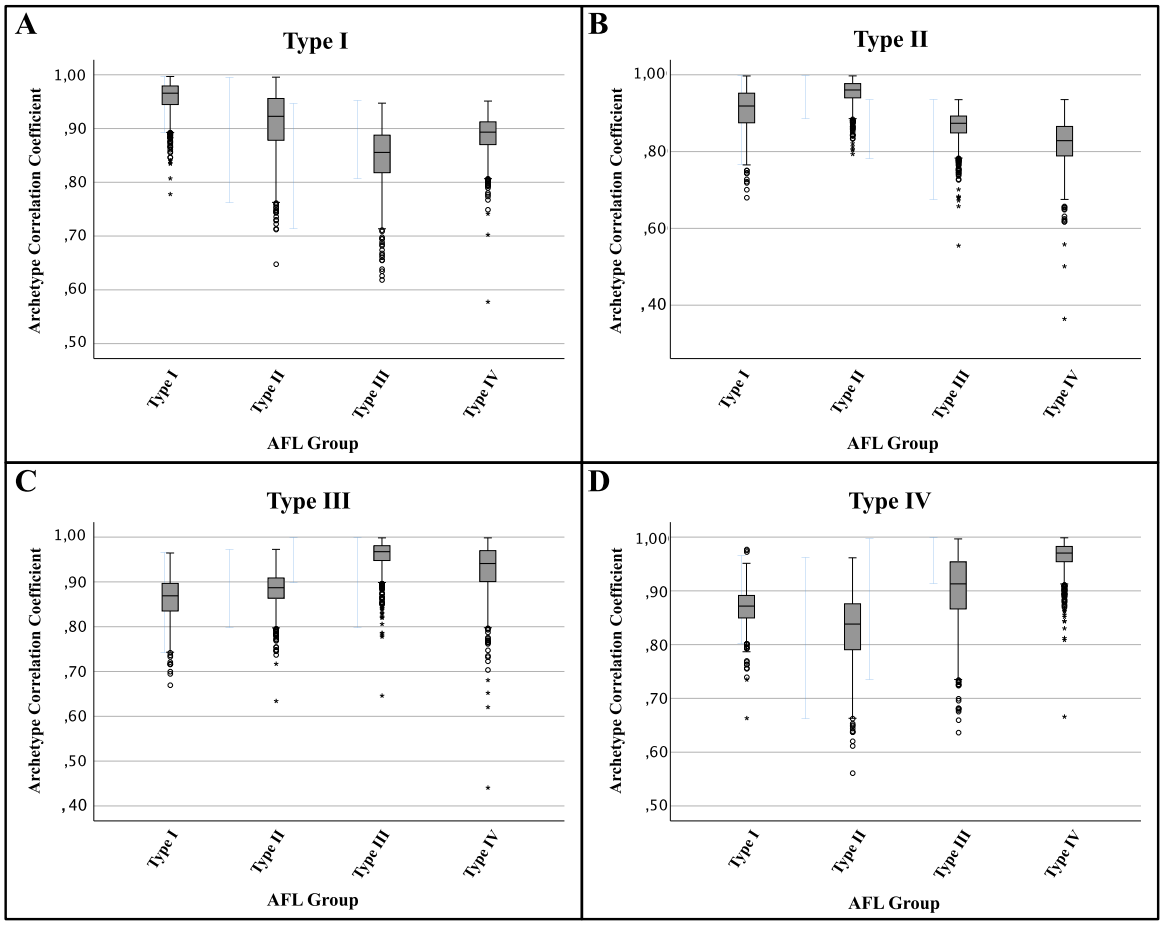

Fig. 5. Box plot of the correlation coefficient of types I to IV with their representative archetypes (A to D correspondingly). Each subfigure represents the correlation of one archetype (created from the training synthetic cases) with all the patients from groups I to IV (the synthetic test cases).

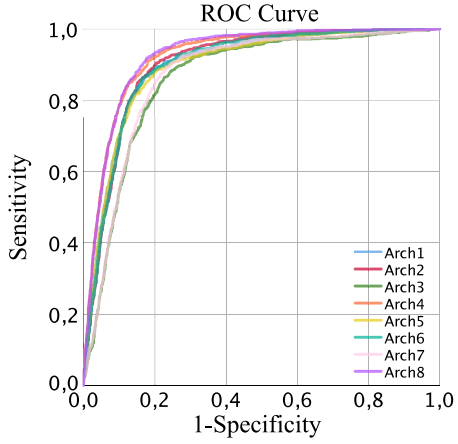

Fig. 6. ROC curves for all patients corresponding to each of the groups when taking into account all the 8000 synthetic patients (A) or the first 4000 in one subgroup (with types I–IV) and the rest in the other (types V–VIII).

5.2.4. Loop complexity

Complexity values for each group are shown in Table 5. The VCG loop described by perimitral MRAT presented higher complexity and longer periods than typical AFL. Moreover, complexity differences between CCW and CW variants from the same MRAT type were also found. Complexity was even higher in the miscellaneous group and in patients with anatomical deformities —a patient with typical AFL and a thoracic malformation (severe pectus excavatum) presented a complexity of 0.68. This patient was discarded from the analysis.

When performing the non-parametric Kruskal–Wallis test over the set of patients grouped as previously described, statistical significance is obtained with a p-value of $p = 0.035$ for the complexity parameter. Thus, the null hypothesis is rejected.

The complexity of the VCG loop was mildly correlated with the atrial cycle length under adenosine effects, with a correlation value of 0.62. These values are also provided in Table 5.

6. Discussion

MRAT may be caused by different macroreentrant circuits which require different ablation approaches. Since there is no

Table 2
AUC for synthetic patients.

	Type I	Type II	Type III	Type IV	Type V	Type VI	Type VII	Type VIII
AUC	0.899	0.902	0.863	0.923	0.895	0.899	0.872	0.926

Table 3
Results of correlation of archetypes with patients from MRAT groups.

	Typical CCW	Typical CW	Perimitral CCW	Perimitral CW	Other types
Typ.CCW Arch.	**0.85 ± 0.03**	0.67 ± 0.11	0.77 ± 0.05	0.73 ± 0.12	0.68 ± 0.14
Typ.CW Arch.	0.68 ± 0.05	**0.95 ± 0.03**	0.66 ± 0.13	0.75 ± 0.04	0.58 ± 0.13
P.CCW Arch.	0.78 ± 0.09	0.63 ± 0.11	**0.87 ± 0.04**	0.68 ± 0.12	0.62 ± 0.18
P.CW Arch.	0.76 ± 0.08	0.75 ± 0.01	0.70 ± 0.12	**0.91 ± 0.02**	0.65 ± 0.17
p-value	0.014	<0.01	<0.01	0.62	N.A.

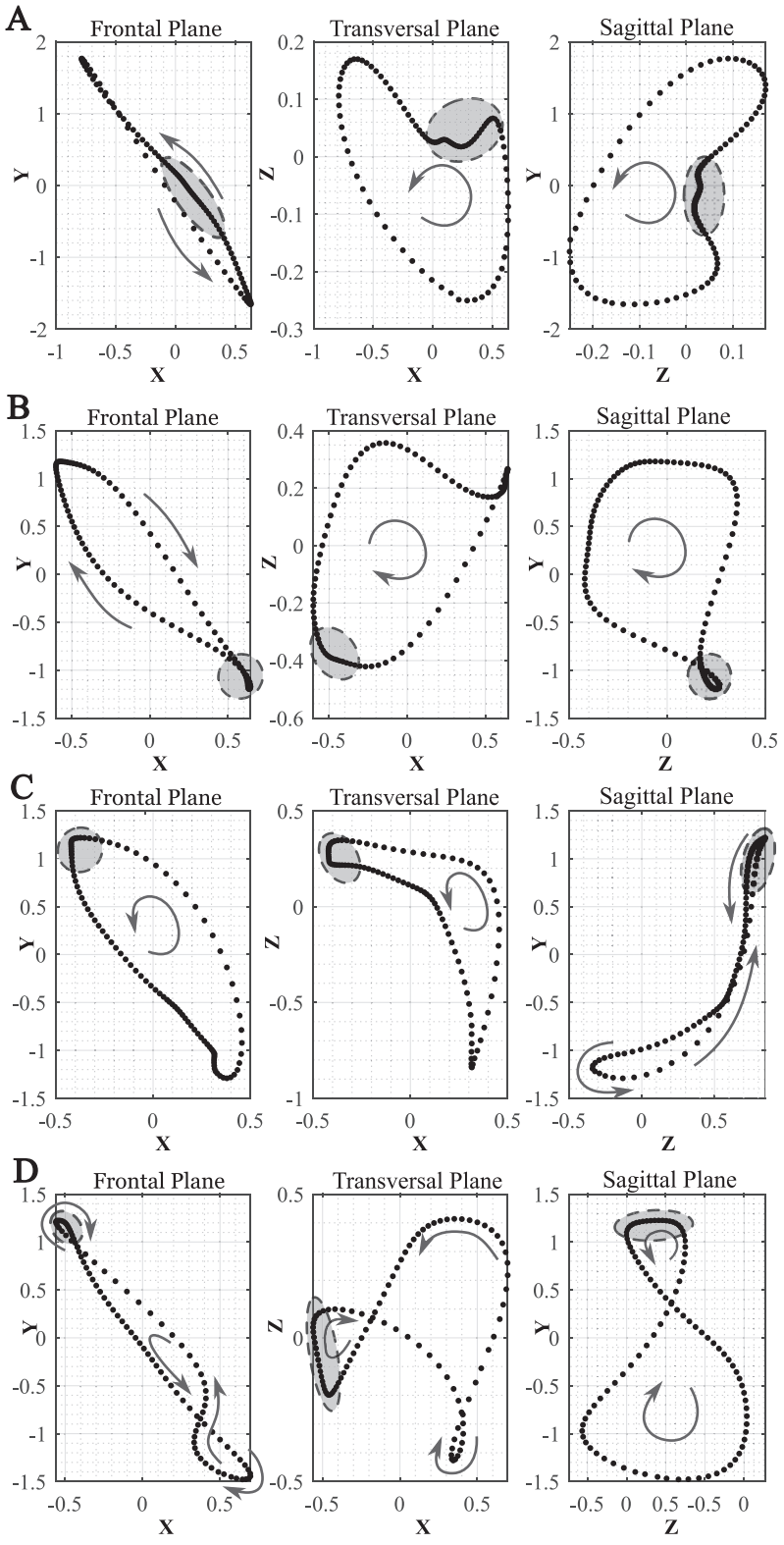

Fig. 7. VCG archetypes for different MRAT group (principal slow velocity region and rotation sense are indicated). A: Typical CCW; B: Typical CW; C: Perimitral CCW; D: Perimitral CW.

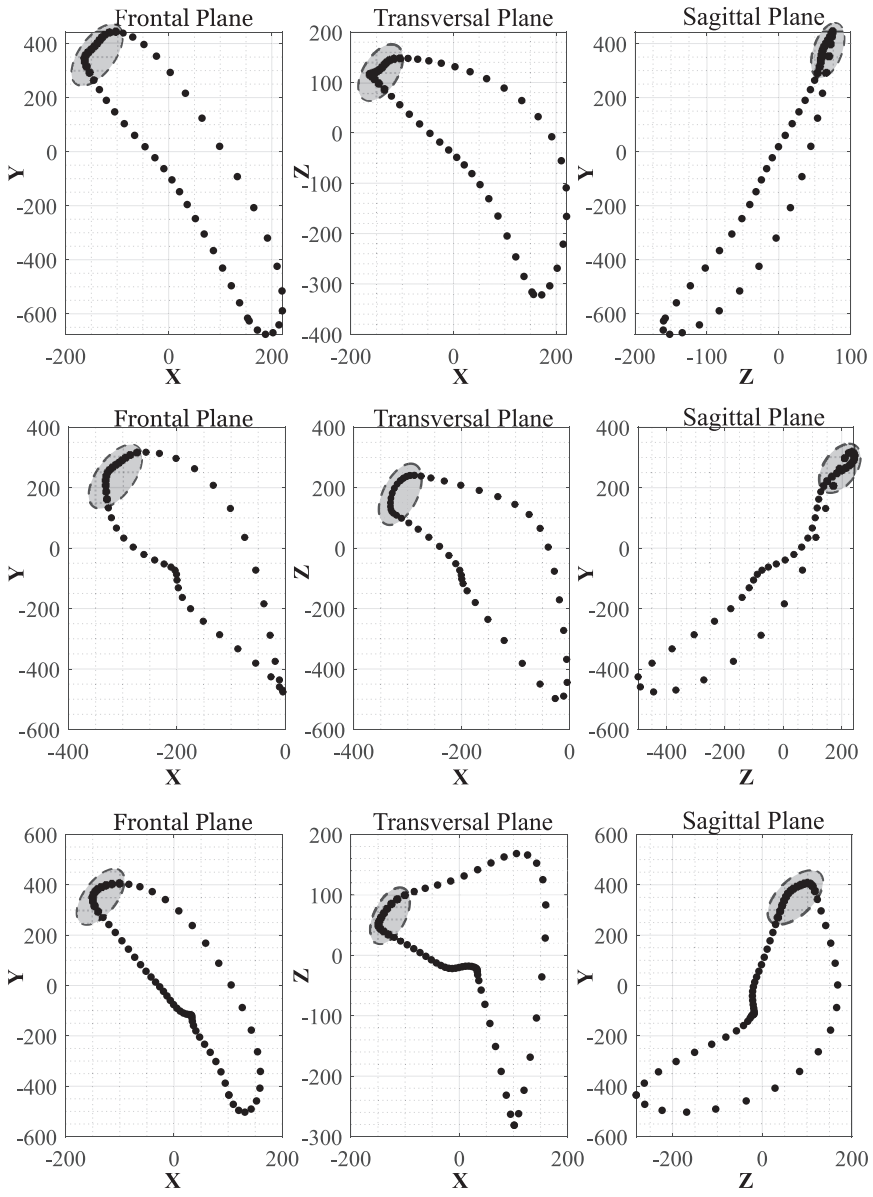

Fig. 8. Examples of VCGs corresponding to CCW Perimitral MRAT (main slow velocity regions are highlighted). Notice the high coincidence with the CCW Perimitral MRAT in Fig. 7C.

Table 4
Results of $\mathbf{TF_{LV}}$, $\mathbf{DF_{LV}}$, $\mathbf{TDR_{LV}}$ and ratio between maximum and minimum velocities V_{max}/V_{min}. *An outlier case with an unusually slow minimum velocity (which led to a V_{max}/V_{min} ratio as high as 267.0) was excluded from the analysis.

	Typ.CCW	Typ.CW	P.CCW	P.CW	Other	Overall
$\mathbf{TF_{LV}}$	0.41 ± 0.04	0.18 ± 0.12	0.30 ± 0.14	0.21 ± 0.19	0.43 ± 0.18	0.32 ± 0.16
$\mathbf{DF_{LV}}$	0.18 ± 0.03	0.08 ± 0.06	0.12 ± 0.06	0.10 ± 0.14	0.17 ± 0.06	0.14 ± 0.07
$\mathbf{TDR_{LV}}$	2.24 ± 0.30	2.30 ± 0.26	2.47 ± 0,37	3.23 ± 1.54	2.46 ± 0.40	2.47 ± 0.59
V_{max}/V_{min}	25.80 ± 20.99	7.876 ± 2.64	15.03 ± 5.57	11.92 ± 2.47	19.01* ± 12.68	16.64* ± 12.61

Table 5
Results of arc parameter for all MRAT groups.

	Typ.CCW	Typ.CW	P.CCW	P.CW	Other	Overall
Complexity	0.24 ± 0.05	0.36 ± 0.12	0.45 ± 0.17	0.39 ± 0.11	0.54 ± 0.18	0.43 ± 0.17
Period (ms)	215.50 ± 7.79	245.20 ± 7.37	250.13 ± 12.79	219.00 ± 11.85	275.89 ± 23.01	249.28 ± 8.85

current reliable identification of the MRAT type from the analysis of the ECG, advances on this issue previous to the ablation procedure would be valuable [39]. In this study, a methodology based on the analysis of the atrial VCG loop is proposed, which can be derived from the ECG by means of the Dower's Inverse Transform.

The synthetic VCG generator model strengthens the hypothesis of the importance of slow regions when characterising AFL. Although some overlapping occurs when correlating synthetic VCGs to different archetypes, the high significance and discrimination capacity unveiled by the statistical methods allows us to conclude the importance of the slow regions as the only parameter unique to each group. Furthermore, controlled tests such as correlating around semi-axes shows how correlation highly depends on whether the slow region is fixed or displaced in the space, entailing a significant decrease in this parameter. Also AUCs demonstrate this discriminating capacity between groups I–IV and V–VIII, without the bias of the noticeable difference between the two directions of rotation.

In the real cases, the proposed methodology enables us to find differences between different MRAT types, even between CCW and CW variants of the same MRAT type. This suggests that loops with CCW and CW rotation directions should be treated independently as different groups. Moreover, there was a high similarity between patients belonging to the same MRAT group, with standard deviations below 0.04 in this parameter. These results denote a promising capability for the identification of the MRAT type. This approach is based on the comparison of the VCG loop with a collection of archetypes corresponding to each MRAT variant. To increase the utility of this method, a universal and publicly available dataset of archetypes would be an asset, so that each health centre would not have to recruit a large number of patients to initiate the study. To proceed with the comparison of VCG loops, it should be noted that a normalisation of the same number of samples per atrial cycle is required. Furthermore, loops should be time-aligned. Although in this conceptual study, brute force was applied for this alignment, since the cost function would not show local maxima, a simple maximisation approach, such as the steepest descent method, could be used instead to save computational load. This is not, however, a critical issue, as the number of computations to be run is feasible.

Interestingly, a discretised plot of MRAT VCG loops showed regions with higher density of samples, consistent with the slow-conduction regions responsible for the perpetuation of the macroreentrant circuit. This property of the atrial VCGs has not been reported hitherto. In addition, this may play a key role for the identification of the MRAT type. The velocity profile described by the surface VCG loop showed significant differences along the pathway, with a median of 12.93 for ratios between the fastest and slowest velocity, ranging between 4.55 and 256.95, which confirms the systematic presence of a low velocity region. In those periods with lower velocity, a much longer time is required to cover a similar arc portion in contrast to other instants with higher velocity. In addition to velocity definition measured as voltage increment per cycle unit, the angular velocity would also be of interest, as it may highlight direction changes in sites close to the VCG centre, i.e. with a short turning radius, as if an obstacle were surrounded. Whether this is related to an anatomical or physiological feature is still to be explored.

An important application of this method is the identification of the slow conduction intervals. This would allow a real-time projection to highlight these segments on the signal registered by an exploratory catheter (e.g. the ablation catheter), which would be useful for monitoring whether it is approaching or moving away from the slow conduction region. This would help find the target ablation sites more efficiently. Fig. 9 illustrates an example of a typical AFL, with the 1-2, 3-4 and 5-6 electrode pairs of the multipolar catheter placed on the cavo-tricuspid isthmus. As shown in this figure, once the slow conduction intervals are identified, and due to the periodicity and regularity of the macroreentry mechanisms, these can also be extrapolated to segments where the atrial signal is masked by ventricular components. This is also applicable to patients with a consistent 2:1 AV conduction ratio, where the atrial wave is no longer visible during long periods, which brings tremendous potential to guide the electrophysiological exploration.

Unexpectedly, there were important differences in time and distance fractions during low velocity between CCW and CW variants of the same MRAT type. This raises new questions regarding asymmetries in the conduction properties depending on the rotation direction, which should be answered by electrophysiological studies.

Regarding the complexity of the atrial loop, perimitral MRAT presented more complex patterns, which suggests a longer and more winding pathway to close the loop. This property is even magnified in MRATs with anatomical deformities.

In order to apply this method successfully, an unequivocal atrial signal —i.e. with no ventricular activity— is required. However, the atrioventricular (AV) conduction ratio is often as short as 2:1. Therefore, the atrial signal is overlapped by either the QRS complex or the T wave. Due to the high consistency of atrial loops, even one single loop might be sufficient, which could be captured if longer RR intervals were available. Otherwise, adenosine administration or carotid massage could facilitate obtaining the atrial signal. Nevertheless, specific approaches to retrieve the atrial signal from the ECG would be valuable. Although several approaches have been proposed for atrial fibrillation, they are likely to fail in the case of atrial flutter. Regarding algorithms based on QRS-T cancellation [19,40], as long as the atrial cycles are coupled with the ventricular activity, the atrial signal will be removed as well. On the other hand, methods based on Blind Source Separation [21] are able to extract one projection consistent with the atrial source. However, a single component is still insufficient to project back the VCG, as three (or at least 2) components would be required, rendering those methods useless. Therefore, improved algorithms exploiting either the spatial or temporal properties of the signals —such as projective filtering methods [41] or Periodic Component Analysis (πCA) [42]— are worth developing. Additionally, another strategy based on the estimation and removal of the T-wave in MRAT has been recently proposed [23], which would also be of great interest if it could robustly retrieve a complete atrial cycle in patients with a stable AV conduction ratio of 2:1.

6.1. Study limitations

We are aware of the low number of patients per group involved in this study. Nonetheless, statistically significant results were obtained, which are expected to improve by adding new data, e.g. with further multicentric studies.

Regarding our simulation model, we employed a geometrical approach, as decribed above. Although this allows us full control of the parameters involved and a thorough evaluation of the properties of the methods, it does not arise from a physiological phenomenon. Further studies with in-silico 3D models of atrial activations according to Courtemanche modelling of ionic mechanisms and numerical computation of the VCG by means of the forward problem could provide different patterns associated with different macroreentrant circuits [43]. In turn, the simulated VCG loops could be compared to their corresponding archetypes obtained from real data.

Finally, we are also constrained to the inherent limitations of the system for signal acquisition and cardiac mapping (CARTO®3, Biosense Webster). Novel high density acquisition systems such

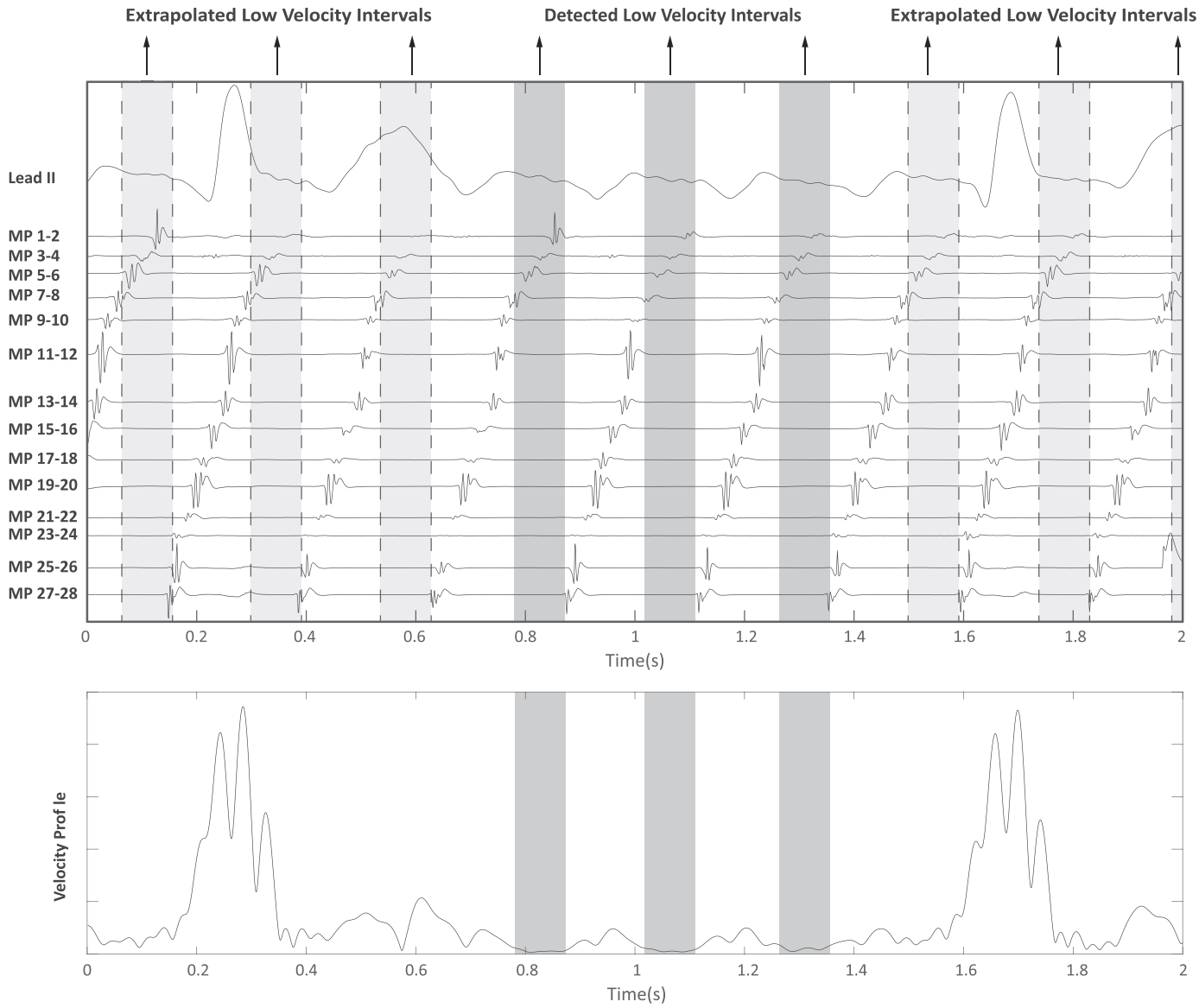

Fig. 9. Slow velocity intervals detected from the velocity profile of a typical AFL (bottom) are highlighted on the temporal EGM sequence (dark grey), and extrapolated to segments with ventricular activity (light grey). These intervals matched with the activation timing at the electrodes located on the CTI (MP 1-2,3-4 and 5-6).

as the Advisor^{TM}HD Grid Mapping Catheter (Abbott Laboratories) or RHYTHMIA HDx^{TM}(Boston Scientific) are able to collect, display and analyse higher resolution data. These techniques constitute very promising alternatives for a better and more accurate characterisation of the electrophysiological substrate and, hence, may provide improved and clinically meaningful information for the management of MRATs [44,45].

7. Conclusions

A non-invasive methodology is proposed to characterise different MRAT circuits from ECG recordings. The proposed method is based on the VCG, and more precisely, on the evaluation of the loop trajectory. This study shows how different VCG loops present some similarities between the same MRAT group. Moreover, this tool reflects sites with slow velocity, consistent with slow conduction regions, prominent in the macroreentrant circuit. The proposed approach can help to better identify the MRAT type in a non-invasive way. Having this information prior to the ablation procedure would be valuable in order to improve the planning and management of medical interventions.

Declaration of Competing Interest

The authors declare that they have no known competing financial interests or personal relationships that could have appeared to influence the work reported in this paper.

Acknowledgements

This work was supported by PID2019-109547RB-I00 (National Research Program, Ministerio de Ciencia e Innovación, Spanish Government), CIBERCV CB16/11/00486 (Instituto de Salud Carlos III) and PROMETEOII/2014/037 (Generalitat Valenciana).

The study adheres to the Declaration of Helsinki, was approved by the 'Comité Ético de Investigación Bioética, Hospital Universitario La Paz', and all subjects gave their informed consent to participate.

Appendix A. VCG loop alignment

Defining each individual loop by the triplet $(\mathbf{X}_k, \mathbf{Y}_k, \mathbf{Z}_k)$, where a bold typeface vector is composed of all time samples and $k = 1 \dots K$, a least square minimisation approach is considered. Unlike the model in Sörnmo [46], each individual loop is simply assumed to be a noisy observation of a time shifted reference loop $(\mathbf{X}^{\{r\}}, \mathbf{Y}^{\{r\}}, \mathbf{Z}^{\{r\}})$. The noise level is assumed to be identical whatever the lead and the patient, providing the simple least square expression:

$$\hat{d}_1, \dots, \hat{d}_K, \hat{\mathbf{X}}^{\{r\}}, \hat{\mathbf{Y}}^{\{r\}}, \hat{\mathbf{Z}}^{\{r\}} = arg \max_{d_1,\dots,d_K, \mathbf{X}^{\{r\}}, \mathbf{Y}^{\{r\}}, \mathbf{Z}^{\{r\}}} (J)$$

with

$$\begin{aligned} J &= \sum_k \left(\left\| \mathbf{X}_k - \mathbf{X}^{\{r\}}_{d_k} \right\|^2 + \left\| \mathbf{Y}_k - \mathbf{Y}^{\{r\}}_{d_k} \right\|^2 + \left\| \mathbf{Z}_k - \mathbf{Z}^{\{r\}}_{d_k} \right\|^2 \right) \\ &= \sum_k \Big(\mathbf{X}_k^T \mathbf{X}_k + \mathbf{Y}_k^T \mathbf{Y}_k + \mathbf{Z}_k^T \mathbf{Z}_k - 2\mathbf{X}_k^T \mathbf{X}^{\{r\}}_{d_k} - 2\mathbf{Y}_k^T \mathbf{Y}^{\{r\}}_{d_k} \\ &\quad -2\mathbf{Z}_k^T \mathbf{Z}^{\{r\}}_{d_k} + \mathbf{X}^{\{r\}T}_{d_k} \mathbf{X}^{\{r\}}_{d_k} + \mathbf{Y}^{\{r\}T}_{d_k} \mathbf{Y}^{\{r\}}_{d_k} + \mathbf{Z}^{\{r\}T}_{d_k} \mathbf{Z}^{\{r\}}_{d_k} \Big) \end{aligned}$$

With this formulation, the shifts d_k's operates on the reference loop. Using the property that each record is a loop, the expression can be replaced and simplified by:

$$\begin{aligned} J = \sum_k \big(&-2\mathbf{X}^T_{k,-d_k} \mathbf{X}^{\{r\}} - 2\mathbf{Y}^T_{k,-d_k} \mathbf{Y}^{\{r\}} - 2\mathbf{Z}^T_{k,-d_k} \mathbf{Z}^{\{r\}} \\ &+ \mathbf{X}^{\{r\}T} \mathbf{X}^{\{r\}} + \mathbf{Y}^{\{r\}T} \mathbf{Y}^{\{r\}} + \mathbf{Z}^{\{r\}T} \mathbf{Z}^{\{r\}} \big) + C \end{aligned}$$

where C stands for a constant. In order to minimise the criteria J the derivation with respect to each reference loop is given by:

$$\frac{\partial J}{\partial \mathbf{X}^{\{r\}}} = \sum_k \left(-2\mathbf{X}_{k,-d_k} + 2\mathbf{X}^{\{r\}} \right)$$

$$\frac{\partial J}{\partial \mathbf{Y}^{\{r\}}} = \sum_k \left(-2\mathbf{Y}_{k,-d_k} + 2\mathbf{Y}^{\{r\}} \right)$$

$$\frac{\partial J}{\partial \mathbf{Z}^{\{r\}}} = \sum_k \left(-2\mathbf{Z}_{k,-d_k} + 2\mathbf{Z}^{\{r\}} \right)$$

Zeroing each expression provides the solutions:

$$\hat{\mathbf{X}}^{\{r\}} = \frac{1}{K} \sum_k \mathbf{X}_{k,-d_k}$$

$$\hat{\mathbf{Y}}^{\{r\}} = \frac{1}{K} \sum_k \mathbf{Y}_{k,-d_k}$$

$$\hat{\mathbf{Z}}^{\{r\}} = \frac{1}{K} \sum_k \mathbf{Z}_{k,-d_k}$$

It can be shown that when replacing these solutions in J we get:

$$\begin{aligned} J &= C - \hat{\mathbf{X}}^{\{r\}T} \hat{\mathbf{X}}^{\{r\}} - \hat{\mathbf{Y}}^{\{r\}T} \hat{\mathbf{Y}}^{\{r\}} - \hat{\mathbf{Z}}^{\{r\}T} \hat{\mathbf{Z}}^{\{r\}} \\ &= C - \|\hat{\mathbf{X}}^{\{r\}}\|^2 - \|\hat{\mathbf{Y}}^{\{r\}}\|^2 - \|\hat{\mathbf{Z}}^{\{r\}}\|^2 \end{aligned}$$

Meaning that the minimisation of J is equivalent to maximise the sum of the energy of the resynchronised averaged leads. That is:

$$\hat{d}_1, \dots, \hat{d}_k = arg \max_{d_1,\dots,d_k} (\|\hat{\mathbf{X}}^{\{r\}}\|^2 + \|\hat{\mathbf{Y}}^{\{r\}}\|^2 + \|\hat{\mathbf{Z}}^{\{r\}}\|^2)$$

We propose using an iterative scheme to get the solution of this maximisation. The delays d_k's are sequentially selected over an interval corresponding to the length of the loop in order to maximise the criteria. After the selection of the last delay d_k the global process is repeated until convergence. Note that using the estimated delays not only the loop are temporally aligned but also the estimated reference loops $\mathbf{X}^{\{r\}}$, $\mathbf{Y}^{\{r\}}$, $\mathbf{Z}^{\{r\}}$ are provided.

Supplementary material

Supplementary material associated with this article can be found, in the online version, at doi:10.1016/j.cmpb.2021.105932

References

[1] E. Herzog, E. Argulian, S.B. Levy, E.F. Aziz, Pathway for the management of atrial fibrillation and atrial flutter, Crit. Pathw. Cardiol. 16 (2) (2017) 47–52.
[2] W. Dresen, P.K. Mason, Atrial flutter after surgical maze: incidence, diagnosis, and management, Curr. Opin. Cardiol. 31 (1) (2016) 57–63.
[3] S.M. Markowitz, G. Thomas, C.F. Liu, J.W. Cheung, J.E. Ip, B.B. Lerman, Approach to catheter ablation of left atrial flutters, J. Cardiovasc. Electrophysiol. 30 (12) (2019) 3057–3067.
[4] C. Butta, A. Tuttolomondo, L. Giarrusso, A. Pinto, Electrocardiographic diagnosis of atrial tachycardia: classification, *p*-wave morphology, and differential diagnosis with other supraventricular tachycardias, Ann. Noninvasive Electrocardiol. 20 (4) (2015) 314–327.
[5] F.G. Cosío, Atrial flutter, typical and atypical: a review, Arrhyth. Electrophysiol. Rev. 6 (2) (2017) 55.
[6] C.-H. Lin, Y.-J. Lin, S.-L. Chang, L.-W. Lo, H.-K. Huang, C.-H. Chiang, S. Allamsetty, J.-N. Liao, F.-P. Chung, Y.-T. Chang, et al., Novel electrophysiological characteristics of atrioventricular nodal continuous conduction curves in atrioventricular nodal re-entrant tachycardia with concomitant cavotricuspid isthmus-dependent atrial flutter, Ep Europace 18 (8) (2016) 1259–1264.
[7] V.Y. See, Organized atrial arrhythmias after cardiac transplantation: the overlooked value of the 12-lead electrocardiogram and cavotricuspid atrial flutter isthmus, J. Heart Lung Transpl. 37 (2) (2018) 192–194.
[8] M. Yokokawa, M.C. Sinno, M. Saeed, R. Latchamsetty, H. Ghanbari, T. Crawford, K. Jongnarangsin, R. Cunnane, F. Pelosi, F. Bogun, et al., The relationship between the *p* wave and local atrial electrogram in predicting conduction block during catheter ablation of cavo-tricuspid isthmus-dependent atrial flutter, J. Interv. Card. Electrophysiol. 53 (2) (2018) 187–193.
[9] M.S. Baccillieri, S. Rizzo, M. De Gaspari, B. Paradiso, G. Thiene, R. Verlato, C. Basso, Anatomy of the cavotricuspid isthmus for radiofrequency ablation in typical atrial flutter, Heart Rhythm. 16 (11) (2019) 1611–1618.
[10] S. Saygi, H. Bastani, N. Drca, P. Insulander, C. Wredlert, J. Schwieler, M. Jensen-Urstad, Impact of cavotricuspid isthmus morphology in cryo versus radiofrequency ablation of typical atrial flutter, Scand. Cardiovasc. J. 51 (2) (2017) 69–73.
[11] G. Peigh, J. Wasserlauf, P. Sattayaprasert, N. Verma, B.P. Knight, Use of the cryoballoon to ablate pulmonary vein-dependent left atrial flutter, Pacing Clin. Electrophysiol. 42 (12) (2019) 1589–1593.
[12] S.-S. Bun, D.G. Latcu, F. Marchlinski, N. Saoudi, Atrial flutter: more than just one of a kind, Eur. Heart J. 36 (35) (2015) 2356–2363.
[13] Y. Rudy, Electrocardiographic imaging (ECGI): a new noninvasive imaging modality for cardiac electrophysiology and arrhythmia, in: Medical Imaging 2006: Physiology, Function, and Structure from Medical Images, 6143, International Society for Optics and Photonics, 2006, p. 614306.
[14] C. Ramanathan, R.N. Ghanem, P. Jia, K. Ryu, Y. Rudy, Noninvasive electrocardiographic imaging for cardiac electrophysiology and arrhythmia, Nat. Med. 10 (4) (2004) 422–428.
[15] J.P. Piccini, Clinical trials in atrial fibrillation: lessons from the box score, 2018.
[16] C. Pedrinazzi, O. Durin, G. Mascioli, A. Curnis, R. Raddino, G. Inama, L. Dei Cas, Atrial flutter: from ECG to electroanatomical 3d mapping, Heart Int. 2 (3-4) (2006) 161.
[17] A.S. Manolis, Contemporary diagnosis and management of atrial flutter, Cardiol. Rev. 25 (6) (2017) 289–297.
[18] P. Milliez, A.W. Richardson, O. Obioha-Ngwu, P.J. Zimetbaum, P. Papageorgiou, M.E. Josephson, Variable electrocardiographic characteristics of isthmus-dependent atrial flutter, J. Am. Coll. Cardiol. 40 (6) (2002) 1125–1132.
[19] F. Castells, C. Mora, J. Rieta, J. Millet, Estimation of atrial fibrillatory wave from single-lead atrial fibrillation electrocardiograms using principal component analysis concepts, Med. Biol. Eng. Comput. 43 (2005) 557–560.
[20] E.K. Roonizi, R. Sassi, An extended Bayesian framework for atrial and ventricular activity separation in atrial fibrillation, IEEE J. Biomed. Health Inform. 21 (6) (2017) 1573–1580.
[21] J.J. Rieta, F. Castells, C. Sánchez, V. Zarzoso, J. Millet, Atrial activity extraction for atrial fibrillation analysis using blind source separation, IEEE Trans. Biomed. Eng. 51 (7) (2004) 1176–1186.
[22] F. Castells, J.J. Rieta, J. Millet, V. Zarzoso, Spatiotemporal blind source separation approach to atrial activity estimation in atrial tachyarrhythmias, IEEE Trans. Biomed. Eng. 52 (2) (2005) 258–267.
[23] V. Jacquemet, B. Dube, R. Nadeau, A.R. LeBlanc, M. Sturmer, G. Becker, T. Kus, A. Vinet, Extraction and analysis of t waves in electrocardiograms during atrial flutter, IEEE Trans. Biomed. Eng. 58 (4) (2010) 1104–1112.
[24] J.-C. Deharo, M. Brignole, R. Guieu, Adenosine hypersensitivity and atrioventricular block, Herzschrittmachertherapie+ Elektrophys. 29 (2) (2018) 166–170.
[25] C.A. Pastore, N. Samesima, H.G. Pereira Filho, N.M.M.d.O. Tobias, B.A. Madaloso, M.E. Facin, Applicability of the electro-vectorcardiogram in current clinical practice, Arq. Bras. Cardiol. 113 (1) (2019) 87–99.
[26] G. Sedaghat, E. Ghafoori, J. Waks, M. Kabir, A. Shvilkin, M. Josephson, L. Tereshchenko, Quantitative assessment of vectorcardiographic loop morphology, J. Electrocardiol. 49 (2016), doi:10.1016/j.jelectrocard.2015.12.014.

[27] S. Choudhuri, T. Ghosal, D.P. Goswami, A. Sengupta, Planarity of the spatial QRS loop of vectorcardiogram is a crucial diagnostic and prognostic parameter in acute myocardial infarction, Med. Hypotheses 130 (2019) 109–251.
[28] D. Oehler, T. Feldman, C. Henrikson, L. Tereshchenko, QRS-T angle: a review, Ann. Noninvasive Electrocardiol. 19 (2014), doi:10.1111/anec.12206.
[29] M.H.K. Azman, O. Meste, K. Kadir, D.G. Latcu, Localizing atrial flutter circuit using variability in the vectorcardiographic loop parameters, in: 2018 Computing in Cardiology Conference (CinC), 45, IEEE, 2018, pp. 1–4.
[30] J. Ng, A.V. Sahakian, W. Fisher, S. Swiryn, A vectorcardiographic approach to understanding the 12-lead electrocardiogram of atrial flutter, in: Computers in Cardiology, 2004, IEEE, 2004, pp. 629–632.
[31] A. Alcaine, M. Mase, A. Cristoforetti, F. Ravelli, G. Nollo, P. Laguna, J.P. Martínez, L. Faes, A multi-variate predictability framework to assess invasive cardiac activity and interactions during atrial fibrillation, IEEE Trans. Biomed. Eng. 64 (5) (2016) 1157–1168.
[32] C.D. Giurcăneanu, I. Tăbuş, Ş. Mereuţă, Using contexts and $R-R$ interval estimation in lossless ECG compression, Comput. Methods Prog. Biomed. 67 (3) (2002) 177–186.
[33] M. Lemay, J.-M. Vesin, A. Van Oosterom, V. Jacquemet, L. Kappenberger, Cancellation of ventricular activity in the ECG: evaluation of novel and existing methods, IEEE Trans. Biomed. Eng. 54 (3) (2007) 542–546.
[34] D. Acharya, A. Rani, S. Agarwal, V. Singh, Application of adaptive Savitzky–Golay filter for eeg signal processing, Perspect. Sci. 8 (2016) 677–679.
[35] A. Aranda, P. Bonizzi, J. Karel, R. Peeters, Performance of Dower's inverse transform and frank lead system for identification of myocardial infarction, in: 2015 37th Annual International Conference of the IEEE Engineering in Medicine and Biology Society (EMBC), IEEE, 2015, pp. 4495–4498.
[36] R. Jaros, R. Martinek, L. Danys, Comparison of different electrocardiography with vectorcardiography transformations, Sensors 19 (14) (2019) 3072.
[37] F. Castells, P. Laguna, L. Sörnmo, A. Bollmann, J. Millet-Roig, Principal component analysis in ECG signal processing, EURASIP J. Adv. Signal Process. (2007).
[38] G. Liu, H. Yang, Multiscale adaptive basis function modeling of spatiotemporal vectorcardiogram signals, IEEE J. Biomed. Health Inform. 17 (2) (2013) 484–492.
[39] M.H.B.K. Azman, Novel pre-interventional atrial flutter localization tool for the improvement of radiofrequency ablation efficacy, COMUE Université Côte d'Azur (2015-2019); Universiti Kuala Lumpur (Malaisie), 2019 Ph.D. thesis.
[40] M. Stridh, L. Sornmo, Spatiotemporal QRST cancellation techniques for analysis of atrial fibrillation, IEEE Trans. Biomed. Eng. 48 (1) (2001) 105–111.
[41] T. Przybyła, M. Kotas, J. Łski, On clustering based nonlinear projective filtering of biomedical signals, Biomed. Signal Process. Control 44 (2018) 237–246, doi:10.1016/j.bspc.2018.04.009.
[42] T. Oesterlein, G. Lenis, A. Luik, C. Schmitt, O. Doessel, Periodic component analysis to eliminate ventricular far field artifacts in unipolar atrial electrograms of patients suffering from atrial flutter, 2014, pp. S162–S165, doi:10.1515/bmt-2014-4067.
[43] G. Luongo, S. Schuler, M.W. Rivolta, O. Doessel, R. Sassi, A. Loewe, Automatic classification of 20 different types of atrial tachycardia using 12-lead ECG signals, EP Europace 22 (Supplement_1) (2020), doi:10.1093/europace/euaa162.048. Euaa162.048
[44] D. Frisch, Identifying a gap in a cavotricuspid isthmus flutter line using the advisor^{TM}HD grid high-density mapping catheter, J. Innov. Card. Rhythm Manag. 10 (2019) 3919–3922, doi:10.19102/icrm.2019.111202.
[45] M. Takigawa, N. Derval, A. Frontera, R. Martin, S. Yamashita, G. Cheniti, K. Vlachos, N. Thompson, T. Kitamura, M. Wolf, G. Massoullie, C.A. Martin, N. Al-Jefairi, S. Amraoui, J. Duchateau, N. Klotz, T. Pambrun, A. Denis, F. Sacher, H. Cochet, M. Hocini, M. Haïssaguerre, P. Jais, Revisiting anatomic macroreentrant tachycardia after atrial fibrillation ablation using ultrahigh-resolution mapping: implications for ablation, Heart Rhythm 15 (3) (2018) 326–333, doi:10.1016/j.hrthm.2017.10.029.
[46] L. Sörnmo, Vectorcardiographic loop alignment and morphologic beat-to-beat variability, IEEE Trans. Biomed. Eng. 45 (1998) 1401–1413.